Journal of Solid Mechanics Vol. 16, No. 2 (2024) pp. 147-167
DOI: 10.60664/jsm.2024.1123602

Research Paper

Dynamic Characteristics of Conical Sandwich Shells with Rheological Fluid-Based Smart Core and Porous Face Sheets

M. Alinejad, S. Jafari Mehrabadi *, M.M. Najafizadeh

Department of Mechanical Engineering, Arak Branch, Islamic Azad University, Arak, Iran

Received 24 June 2024; Received in revised form 31 July 2024; Accepted 15 August 2024

ABSTRACT

This research is devoted to the free vibrational analysis of a truncated conical three-layered sandwich shell with a rheological core and functionally graded (FG) porous face sheets. The rheological core can be either electrorheological elastomer (ERF) or magnetorheological fluid (MRF). The mathematical modeling of the layers of the shell is performed based on the first-order shear deformation theory (FSDT) by including the continuity conditions between the core and two face sheets. Three different porosity distribution patterns are investigated including a uniform one and two FG non-uniform ones. The porosity parameters of these distribution patterns are adjusted to result in the same mass (weight) for all patterns. The governing equations and associated boundary conditions are attained through Hamilton's principle and are solved via a semi-analytical solution to determine the natural frequencies of the shell and corresponding loss factors. This semi-analytical solution includes an exact solution in the circumferential direction followed by an approximate solution in the meridional direction via the differential quadrature method (DQM). The effects of several parameters on the natural frequencies and loss factors are examined such as intensity of the magnetic and electric fields, thickness of the rheological core, distribution pattern and porosity parameter of the FG porous face sheets, and the boundary conditions. Numerical results show that the sandwich shell with ERF core benefits from higher natural frequencies rather than the sandwich shell with MRF core. However, the sandwich shell with MRF core benefits from higher loss factors rather than the sandwich shell with ERF core.

Keywords: Free vibration; Sandwich shell; Conical shell; Rheological materials; Porous materials.

*Corresponding author. Tel.: +98 86 33412563; Fax: +98 86 33412563.
E-mail address: sa.jafari@iau.ac.ir (S. Jafari Mehrabadi)

1 INTRODUCTION

SMART materials with controllable damping and stiffness characteristics such as piezoelectric materials [1-3], magnetostrictive materials [4, 5], self-healing polymers [6], and rheological materials [7, 8] have drawn attention from researchers and engineers. Electrorheological fluid (ERF) and magnetorheological fluids (MRF) are two well-known smart materials which their damping and stiffness characteristics can be easily affected by applied electric and magnetic fields. These smart fluids contain suspended electrically and magnetically polarizable micro-particles which are sensitive to applied electric and magnetic fields. When such fluids are exposed to electric and magnetic fields, the arrangement of the micro-particles changes which influences the damping and stiffness characteristics of the fluid. It should be noted that when the applied electric or magnetic field is removed, the mechanical properties of ERF and MRF are restored.

Owing to the above-mentioned unique, smart, and controllable mechanical properties, a fair number of papers have been presented associated with the dynamic analysis of the sandwich structures with ERF or MRF cores. An experimental study was presented by Nagiredla et al. [9] to measure the natural frequencies and loss factors of cantilever sandwich beams with MRF cores. They provided benchmark results to be used by other researchers to validate their theoretical works. Srinivasa et al. [10] examined the free vibrational behavior of cantilever sandwich beams with MRF cores. For two cases including partially or fully filled MRF cores, they studied the effects of the magnetic field on the natural frequencies and loss factors. Eshaghi [11] studied the aeroelastic stability (flutter) behavior of a sandwich plate with an MRF core exposed to supersonic fluid flow. In a similar work, He studied the aeroelastic stability analysis of a circular annular sandwich plate with an MRF core [12]. In both works, He tried to improve the aeroelastic stability of the plates by applying a magnetic field to the MRF core. The free vibration characteristics of a sandwich beam with an ERF core and two nanocomposite polymeric face sheets reinforced with carbon nanotubes (CNTs) were investigated by Ghorbanpour Arani et al. [13]. In a similar work, Ghorbanpour Arani and Jamali [14] studied the free vibration analysis of a cylindrical sandwich shell with an ERF core and CNT-reinforced face sheets. In both works presented in Refs. [13, 14]. The authors focused on the influences of the applied electric field and mass fraction of the CNTs on the natural frequencies and loss factors. Gholamzadeh Babaki and Shakouri [15] studied the free and forced vibration analyses of a sandwich plate with an ERF core and two face sheets fabricated from metal-ceramic functionally graded material (FGM). They inspected the influences of the applied electric field on the natural frequencies, loss factors, and dynamic response of the plate. Aboutalebi et al. [16] examined the nonlinear free vibration analysis of circular, annular, and sector sandwich plates MRF cores. The dependencies of the natural frequencies and loss factors on the applied magnetic field were studied by them. Soroor et al. [17] examined the free vibration analysis of a sandwich beam with an MRF core and two axially functionally graded face layers. The effects of the applied magnetic field and the FG power-law index on the natural frequencies and loss factors were studied by them. Ebrahimi and Sedighi [18] studied the wave propagation analysis of a rectangular sandwich plate with an MRF core. They focused on the influences of the applied magnetic field on the wave dispersion characteristics of the plate. Keshavarzian et al. [19] made a comparison between the application of ERF and MRF cores in the damping behavior of sandwich panels. They tried to minimize the oscillations of the panel with these smart materials. In another work, they studied the nonlinear free vibrational behavior of a sandwich panel with an ERF core [20]. They examined the dependency of the natural frequencies and loss factors on the thickness of the ERF core. Shahali et al. [21] presented a semi-analytical solution to examine the free vibration analysis of a sandwich cylindrical shell with an ERF core and two FGM face sheets. They studied the influences of the FG power-law index and the applied electric field on the natural frequencies and loss factors. The wave propagation characteristics of a sandwich beam with an ERF core were investigated by Shariati et al. [22]. The dependency of the wave dispersion characteristics of the beam on the applied electric field was examined by them. Khorshidi et al. [23] studied the nonlinear free vibration analysis of a sandwich plate with an ERF core coupled to quiescent fluid. The dependency of the natural frequencies and loss factors on the applied electric field and fluid parameters were investigated by them. Farahani et al. [24] studied the size-dependent free vibration analysis of a sandwich cylindrical micro-shell with an MRF core and porous face sheets. The impacts of the applied magnetic field and the length scale parameter on the natural frequencies and loss factors were examined by them.

To the best knowledge of the authors, the presented work is the first paper regarding the free vibrational analysis of a truncated conical sandwich shell with a rheological core (either ERF or MRF) and FG porous face sheets. The specific objective of the present work is to see how the natural frequencies and loss factors of a conical sandwich shell with either ERF or MRF are affected by applying either electric or magnetic fields. The impacts of several parameters on the natural frequencies and loss factors are examined such as the thickness of the Rheological core and FG porous face sheets, applied magnetic field density, boundary conditions, mass fraction of the CNTs, porosity parameter, and distribution of the pores. Due to the wide usage of conical shells in aerospace structures, the results of the presented work can be utilized in the design, analysis, and optimization of future aerospace structures. It is noteworthy that owing to the porous face sheets, the investigated sandwich structure is a low-weight one which is appropriate for an aerospace structure. Also, by variation of the stiffness and damping of the shell through its smart core, the aeroelastic stability of the structure can be improved [25] which is very crucial for aerospace structures exposed to supersonic fluid flow.

2 MATHEMATICAL MODELING

2.1 Description

As Figure 1 shows, a truncated conical sandwich shell of length L, semi-vertex angle λ, small mean radius a, and large mean radius b is considered. h_2 stands for the thickness of the rheological core and h_1 and h_3 are the thickness of the top and bottom FG porous face sheets.

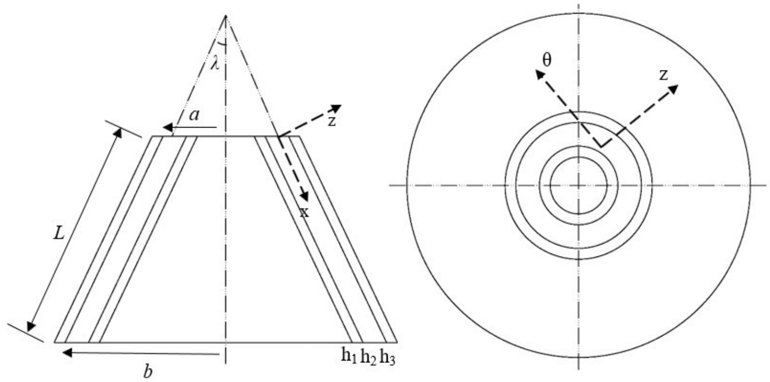

Fig. 1
Description of the problem.

2.2 Material Properties

2.2.1 Rheological core

As a basic assumption, it is supposed that the rheological core does not bear remarkable normal stress and it bears only the shear components of the stress in the thickness direction. Thus, the stress tensor in the rheological core can be described as follows [26]:

$$\begin{Bmatrix} \sigma_{xz}^{(2)} \\ \sigma_{\theta z}^{(2)} \end{Bmatrix} = G_c \begin{Bmatrix} \gamma_{xz}^{(2)} \\ \gamma_{\theta z}^{(2)} \end{Bmatrix}, \tag{1}$$

in which $\gamma_{xz}^{(2)}$ and $\gamma_{\theta z}^{(2)}$ represent shear components of the stress at the rheological core, and as described in Eqn. (2), G_c is a complex value known as the complex shear modulus of the rheological core [27]:

$$G_c = G' + G''j = G_0\left(1 + j\eta_0\right), \tag{2}$$

where j^2=-1 and G_0 and η_0 are called the shear storage modulus and loss factor of the rheological material, sequentially. These parameters are depended on the intensity of the magnetic (B) or electric (E) fields. In this paper, an ERF and an MRF are selected which their complex shear modulus in Pa vary as follows:

ERF [25, 28]:

$$G'\left(E\right) = 15000E^2, \quad G''\left(E\right) = 6900. \tag{3.a}$$

MRF [29]:

$$G'(B) = -3.3691B^2 + 4997.5B + 873000, \quad G''(B) = -0.9B^2 + 812.4B + 185500. \tag{3.b}$$

In Eqn. (3) E indicates the intensity of the electric field in kV/mm in the range $0 \le E \le 2.5$ kV/mm, and in Eqn. (4) B represents the intensity of the magnetic field in Gauss (G) in the range $0 \le B \le 500$ G. The density of the selected ERF and MRF are ρ_c=1700 kg/m^3 and ρ_c=3500 kg/m^3, respectively.

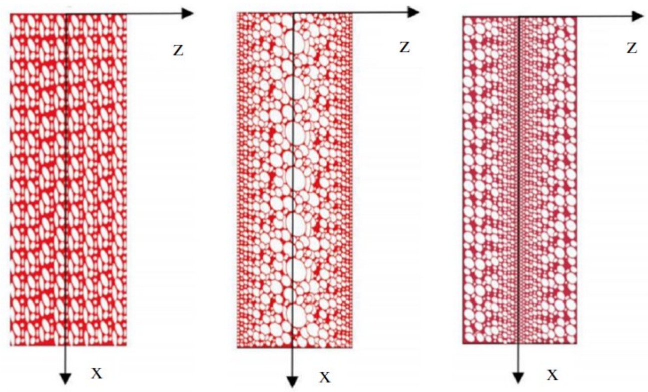

(a) UD (b) SI (c) SII

Fig. 2
Porosity distribution patterns in the face sheets [36].

2.2.2 Porous face sheets

As Figure 2 shows, three porosity distribution patterns are considered in the current work for the porous face layers including a uniform pattern (UD) and two non-uniform symmetric patterns (SI and SII). The elastic modulus of the FG porous core varies along thickness direction as [36]

$$\begin{aligned} &\text{UD:} && \frac{E_i(z_i)}{E_0} = 1 - \eta_0, \\ &\text{SI:} && \frac{E_i(z_i)}{E_0} = 1 - \eta_1 \cos\left(\frac{\pi z_i}{h_i}\right), \qquad i = 1,3. \\ &\text{SII:} && \frac{E_i(z_i)}{E_0} = 1 - \eta_2 \left[1 - \cos\left(\frac{\pi z_i}{h_i}\right)\right], \end{aligned} \tag{4}$$

in which E_0 shows the elastic modulus of the material with no porosity and η_0, η_1, and η_2 are known as the porosity parameters which show the volume of the pores in comparison with the volume of the whole material. It is assumed that the Poisson's ratio is not affected by the pores.

To provide a fair comparison between these porosity distribution patterns, it is more logical to adjust the porosity parameters to provide the same value of mass (weight). The relation below is presented in Refs. [36,37] between the density (ρ_i) and the elastic modulus of a porous material:

$$\frac{\rho_i(z_i)}{\rho_0} = \left[\frac{E_i(z_i)}{E_0}\right]^{\frac{1}{2.73}}. \tag{5}$$

where ρ_0 shows the density of the material with no pore.
By selecting the distribution pattern SI as the base case, the mass equalization of the ith porous face sheet can be expressed as follows:

$$\int_0^{0.5h_i} \rho_0 \left[1 - \eta_1 \cos\left(\frac{\pi z_i}{h_i}\right)\right]^{\frac{1}{2.73}} dz_i = \int_0^{0.5h_i} \rho_0 (1 - \eta_0)^{\frac{1}{2.73}} dz_i, \tag{6}$$

$$\int_0^{0.5h_i} \rho_0 \left[1-\eta_1 \cos\left(\frac{\pi z_i}{h_i}\right)\right]^{\frac{1}{2.73}} dz_i = \int_0^{0.5h_i} \rho_0 \left\{1-\eta_2 \left[1-\cos\left(\frac{\pi z_i}{h_i}\right)\right]\right\}^{\frac{1}{2.73}} dz_i.$$

For some selected values of the porosity parameter e_1, the corresponding values of the porosity parameters η_0 and η_2 are presented in Table 1. The following relations describe the values presented in this table [38]:

$$\eta_0 = 0.6362\eta_1 + 0.122\eta_1^2 - 0.6708\eta_1^3 + 2.278\eta_1^4 - 3.417\eta_1^5 + 1.944\eta_1^6,$$
$$\eta_2 = 1.732\eta_1 - 0.009286\eta_1^2 - 0.4269\eta_1^3. \quad (7)$$

Table 1
Adjusting the porosity parameters [36].

SI	e_1	0	0.1	0.2	0.3	0.4	0.5	0.6
UD	e_0	0	0.0640	0.1287	0.1942	0.2609	0.3289	0.3988
SII	e_2	0	0.1734	0.3426	0.5065	0.6637	0.8112	0.9432

2.3 Governing equations and boundary conditions

According to the FSDT, the relation below describes the displacement field [30, 31]:

$$\hat{u}_i(t,x,\theta,z) = u_i(t,x,\theta) + z_i\varphi_i(t,x,\theta),$$
$$\hat{v}_i(t,x,\theta,z) = v_i(t,x,\theta) + z_i\psi_i(t,x,\theta), \quad i=1,2,3 \quad (8)$$
$$\hat{w}_i(t,x,\theta,z) = w(t,x,\theta),$$

where $\hat{u}_i$, $\hat{v}_i$ and $\hat{w}_i$ show the displacement components along x, θ, and z, directions, sequentially; u_i, v_i and w are the corresponding components of displacement at the middle surface of each layer (z_i=0); and φ_i and ψ_i represent the rotations about θ- and x-axes, respectively.

The continuity of displacement between the core and face sheets can be stated as follows [7]:

$$\hat{u}_2(t,x,\theta,-0.5h_2) = \hat{u}_1(t,x,\theta,0.5h_1), \quad \hat{v}_2(t,x,\theta,-0.5h_2) = \hat{v}_1(t,x,\theta,0.5h_1),$$
$$\hat{u}_2(t,x,\theta,0.5h_2) = \hat{u}_3(t,x,\theta,-0.5h_3), \quad \hat{v}_2(t,x,\theta,0.5h_2) = \hat{v}_3(t,x,\theta,-0.5h_3). \quad (9)$$

By inserting Eqn. (8) into Eqn. (9), the following relations can be obtained:

$$u_2 = 0.5(u_1+u_3) + 0.25(h_1\varphi_1 - h_3\varphi_3), \quad v_2 = 0.5(v_1+v_3) + 0.25(h_1\psi_1 - h_3\psi_3),$$
$$\varphi_2 = h_2^{-1}(u_3-u_1) - 0.5h_2^{-1}(h_1\varphi_1 + h_3\varphi_3), \quad \psi_2 = h_2^{-1}(v_3-v_1) - 0.5h_2^{-1}(h_1\psi_1 + h_3\psi_3). \quad (10)$$

For a conical shell, components of the strain are described as follows [32, 33]:

$$\begin{Bmatrix} \varepsilon_{xx}^{(i)} \\ \varepsilon_{\theta\theta}^{(i)} \\ \gamma_{x\theta}^{(i)} \end{Bmatrix} = \begin{Bmatrix} \dfrac{\partial u_i}{\partial x} \\ \dfrac{1}{r_i}\left(u_i \sin\lambda + \dfrac{\partial v_i}{\partial \theta} + w\cos\lambda\right) \\ \dfrac{\partial v_i}{\partial x} + \dfrac{1}{r_i}\left(\dfrac{\partial u_i}{\partial \theta} - v_i \sin\lambda\right) \end{Bmatrix} + z_i \begin{Bmatrix} \dfrac{\partial \varphi_i}{\partial x} \\ \dfrac{1}{r_i}\left(\varphi_i \sin\lambda + \dfrac{\partial \psi_i}{\partial \theta}\right) \\ \dfrac{\partial \psi_i}{\partial x} + \dfrac{1}{r_i}\left(\dfrac{\partial \varphi_i}{\partial \theta} - \psi_i \sin\lambda\right) \end{Bmatrix}, \quad (11)$$
$$\varepsilon_{zz}^{(i)} = 0, \quad \gamma_{xz}^{(i)} = \varphi_i + \frac{\partial w}{\partial x}, \quad \gamma_{\theta z}^{(i)} = \psi_i + \frac{1}{r_i}\left(\frac{\partial \hat{w}}{\partial \theta} - v_i\cos\lambda\right).$$

where, as described in Eqn. (12), r_i is the mean radius of the ith layer of the shell:

$$r_2 = a + x\sin\lambda, \quad r_1 = r_2 - 0.5(h_1+h_2)\sec\lambda, \quad r_3 = r_2 + 0.5(h_2+h_3)\sec\lambda. \quad (12)$$

The components of stress in the rheological core are described in Eqn. (2). The following equations describe the components of stress in the FG face sheets [34, 35]:

$$\begin{Bmatrix} \sigma_{xx}^{(i)} \\ \sigma_{\theta\theta}^{(i)} \\ \sigma_{\theta z}^{(i)} \\ \sigma_{xz}^{(i)} \\ \sigma_{x\theta}^{(i)} \end{Bmatrix} = \begin{bmatrix} C_{11}^{(i)} & C_{12}^{(i)} & 0 & 0 & 0 \\ C_{12}^{(i)} & C_{22}^{(i)} & 0 & 0 & 0 \\ 0 & 0 & k_s C_{44}^{(i)} & 0 & 0 \\ 0 & 0 & 0 & k_s C_{55}^{(i)} & 0 \\ 0 & 0 & 0 & 0 & C_{66}^{(i)} \end{bmatrix} \begin{Bmatrix} \varepsilon_{xx}^{(i)} \\ \varepsilon_{\theta\theta}^{(i)} \\ \gamma_{\theta z}^{(i)} \\ \gamma_{xz}^{(i)} \\ \gamma_{x\theta}^{(i)} \end{Bmatrix}, \quad i = 1,3 \tag{13}$$

where k_s=5/6 is the shear correction factor and

$$C_{11}^{(i)} = C_{22}^{(i)} = \frac{E_i}{1-\nu_i^2}, \quad C_{12}^{(i)} = \nu_i C_{11}^{(i)}, \quad C_{44}^{(i)} = C_{55}^{(i)} = C_{66}^{(i)} = \frac{E_i}{2(1+\nu_i)}. \tag{14}$$

According to Hamilton's principle, the governing equations and boundary conditions can be derived through the relation below [36, 37]:

$$\int_{t_1}^{t_2} (\delta T - \delta U + \delta W) dt = 0, \tag{15}$$

where δ is the well-known variational operator, $[t_1,t_2]$ represents an arbitrary time interval, U shows the strain energy of the shell, T indicates the kinetic energy of the shell, and W stands for the work done by non-conservative loads.

The kinetic energy of the shell is described as follows [36]:

$$T = 0.5\sum_{i=1}^{3} \iiint_{V_i} \rho_i \left[\left(\frac{\partial \hat{u}_i}{\partial t}\right)^2 + \left(\frac{\partial \hat{v}_i}{\partial t}\right)^2 + \left(\frac{\partial \hat{w}_i}{\partial t}\right)^2 \right] dV_i. \tag{16}$$

in which [38]

$$\iiint_{V_i} (\ ) dV_i = \iint_{S_i} \int_{-0.5h_i}^{0.5h_i} (\ ) dz_i dS_i, \tag{17}$$

where S_i represents the surface of the ith shell at its middle surface (z_i=0).

Utilizing Eqs. (16) and (17) and applying the variational operator, the variation of the kinetic energy can be described as follows:

$$\delta T = \sum_{i=1}^{3} \iint_{S_i} \left[I_0^{(i)} \left(\frac{\partial u_i}{\partial t}\frac{\partial \delta u_i}{\partial t} + \frac{\partial v_i}{\partial t}\frac{\partial \delta v_i}{\partial t} + \frac{\partial w}{\partial t}\frac{\partial \delta w}{\partial t} \right) + I_2^{(i)} \left(\frac{\partial \varphi_i}{\partial t}\frac{\partial \delta \varphi_i}{\partial t} + \frac{\partial \psi_i}{\partial t}\frac{\partial \delta \psi_i}{\partial t} \right) \right] dS_i. \tag{18}$$

where

$$\begin{Bmatrix} I_0^{(i)} \\ I_2^{(i)} \end{Bmatrix} = \int_{-0.5h_i}^{0.5h_i} \rho_i(z_i) \begin{Bmatrix} 1 \\ z_i^2 \end{Bmatrix} dz_i. \tag{19}$$

The strain energy of the shell is described as follows [36]:

$$U = 0.5\sum_{i=1}^{3} \iiint_{V_i} \left(\sigma_{xx}^{(i)}\varepsilon_{xx}^{(i)} + \sigma_{\theta\theta}^{(i)}\varepsilon_{\theta\theta}^{(i)} + \sigma_{\theta z}^{(i)}\gamma_{\theta z}^{(i)} + \sigma_{xz}^{(i)}\gamma_{xz}^{(i)} + \sigma_{x\theta}^{(i)}\gamma_{x\theta}^{(i)} \right) dV_i, \tag{20}$$

By applying the variational operator, the variation of the strain energy can be presented as follows:

$$\delta U = \sum_{i=1}^{3} \iiint_{V_i} \left(\sigma_{xx}^{(i)}\delta\varepsilon_{xx}^{(i)} + \sigma_{\theta\theta}^{(i)}\delta\varepsilon_{\theta\theta}^{(i)} + \sigma_{\theta z}^{(i)}\delta\gamma_{\theta z}^{(i)} + \sigma_{xz}^{(i)}\delta\gamma_{xz}^{(i)} + \sigma_{x\theta}^{(i)}\delta\gamma_{x\theta}^{(i)} \right) dV_i. \tag{21}$$

Utilizing Eqn. (17) and considering the following definitions for the stress resultants:

$$\begin{Bmatrix} N_{xx}^{(i)} \\ N_{\theta\theta}^{(i)} \\ N_{x\theta}^{(i)} \end{Bmatrix} = \int_{-\frac{h_i}{2}}^{\frac{h_i}{2}} \begin{Bmatrix} \sigma_{xx}^{(i)} \\ \sigma_{\theta\theta}^{(i)} \\ \sigma_{x\theta}^{(i)} \end{Bmatrix} dz_i, \quad \begin{Bmatrix} M_{xx}^{(i)} \\ M_{\theta\theta}^{(i)} \\ M_{x\theta}^{(i)} \end{Bmatrix} = \int_{-\frac{h_i}{2}}^{\frac{h_i}{2}} \begin{Bmatrix} \sigma_{xx}^{(i)} \\ \sigma_{\theta\theta}^{(i)} \\ \sigma_{x\theta}^{(i)} \end{Bmatrix} z_i dz_i, \quad \begin{Bmatrix} Q_{\theta z}^{(i)} \\ Q_{xz}^{(i)} \end{Bmatrix} = \int_{-\frac{h_i}{2}}^{\frac{h_i}{2}} \begin{Bmatrix} \sigma_{\theta z}^{(i)} \\ \sigma_{xz}^{(i)} \end{Bmatrix} dz_i, \tag{22}$$

Eqn. (21) can be represented as

$$\begin{aligned} \delta U = \sum_{i=1}^{3} \iint_{S_i} \Bigg\{ & N_{xx}^{(i)} \frac{\partial \delta u_i}{\partial x} + \frac{N_{\theta\theta}^{(i)}}{r_i} \left(\delta u_i \sin\lambda + \frac{\partial \delta v_i}{\partial \theta} + \delta w \cos\lambda \right) + N_{x\theta}^{(i)} \left[\frac{\partial \delta v_i}{\partial x} + \frac{1}{r_i} \left(\frac{\partial \delta u_i}{\partial \theta} - \delta v_i \sin\lambda \right) \right] \\ & + M_{xx}^{(i)} \frac{\partial \delta \varphi_i}{\partial x} + \frac{M_{\theta\theta}^{(i)}}{r_i} \left(\delta \varphi_i \sin\lambda + \frac{\partial \delta \psi_i}{\partial \theta} \right) + M_{x\theta}^{(i)} \left[\frac{\partial \delta \psi_i}{\partial x} + \frac{1}{r_i} \left(\frac{\partial \delta \varphi_i}{\partial \theta} - \delta \psi_i \sin\lambda \right) \right] \\ & + Q_{xz}^{(i)} \left(\delta \varphi_i + \frac{\partial \delta w}{\partial x} \right) + Q_{\theta z}^{(i)} \left[\delta \psi_i + \frac{1}{r_i} \left(\frac{\partial \delta w}{\partial \theta} - \delta v_i \cos\lambda \right) \right] \Bigg\} dS_i. \end{aligned} \tag{23}$$

By inserting Eqns. (1), (11), and (13) into Eqn. (22), one can find the relations below:

$$\begin{aligned}
&\begin{Bmatrix} N_{xx}^{(i)} \\ N_{\theta\theta}^{(i)} \end{Bmatrix} = \begin{bmatrix} A_{11}^{(i)} & A_{12}^{(i)} \\ A_{12}^{(i)} & A_{22}^{(i)} \end{bmatrix} \begin{Bmatrix} \dfrac{\partial u_i}{\partial x} \\ \dfrac{1}{r_i}\left(u_i \sin\lambda + \dfrac{\partial v_i}{\partial \theta} + w\cos\lambda \right) \end{Bmatrix}, \quad \begin{Bmatrix} M_{xx}^{(i)} \\ M_{\theta\theta}^{(i)} \end{Bmatrix} = \begin{bmatrix} D_{11}^{(i)} & D_{12}^{(i)} \\ D_{12}^{(i)} & D_{22}^{(i)} \end{bmatrix} \begin{Bmatrix} \dfrac{\partial \varphi_i}{\partial x} \\ \dfrac{1}{r_i}\left(\varphi_i \sin\lambda + \dfrac{\partial \psi_i}{\partial \theta} \right) \end{Bmatrix}, \\
&N_{x\theta}^{(i)} = A_{66}^{(i)} \left[\frac{\partial v_i}{\partial x} + \frac{1}{r_i}\left(\frac{\partial u_i}{\partial \theta} - v_i \sin\lambda \right) \right], \quad M_{x\theta}^{(i)} = D_{66}^{(i)} \left[\frac{\partial \psi_i}{\partial x} + \frac{1}{r_i}\left(\frac{\partial \varphi_i}{\partial \theta} - \psi_i \sin\lambda \right) \right], \\
&Q_{xz}^{(i)} = A_{55}^{(i)} \left(\varphi_i + \frac{\partial w}{\partial x} \right), \quad Q_{\theta z}^{(i)} = A_{44}^{(i)} \left[\psi_i + \frac{1}{r_i}\left(\frac{\partial w}{\partial \theta} - v_i \cos\lambda \right) \right],
\end{aligned} \tag{24}$$

where

$$\begin{Bmatrix} A_{pq}^{(i)} \\ D_{pq}^{(i)} \end{Bmatrix} = \int_{-0.5h_i}^{0.5h_i} C_{pq}^{(i)}(z_i) \begin{Bmatrix} 1 \\ z_i^2 \end{Bmatrix} dz_i, \quad A_{tt}^{(i)} = k_s \int_{-0.5h_i}^{0.5h_i} C_{tt}^{(i)}(z_i)\, dz_i, \quad \begin{matrix} i = 1,3 \\ p,q = 1,2,6 \\ t = 4,5 \end{matrix} \tag{25}$$

In the free vibration analysis of a structure, there is no external load applied to the structure (δW=0). Thus, by inserting Eqns. (18) and (23) into Eqn. (15), the following governing equations can be attained:

$$\begin{aligned}
&\frac{\partial N_{xx}^{(1)}}{\partial x} + \frac{\sin\lambda}{r_1}\left(N_{xx}^{(1)} - N_{\theta\theta}^{(1)} \right) + \frac{1}{r_1}\frac{\partial N_{x\theta}^{(1)}}{\partial \theta} + \frac{r_2}{r_1}\frac{Q_{xz}^{(2)}}{h_2} - I_0^{(1)}\frac{\partial^2 u_1}{\partial t^2} - \frac{r_2}{r_1}\left(\frac{I_0^{(2)}}{2}\frac{\partial^2 u_2}{\partial t^2} - \frac{I_2^{(2)}}{h_2}\frac{\partial^2 \varphi_2}{\partial t^2} \right) = 0, \\
&\frac{1}{r_1}\frac{\partial N_{\theta\theta}^{(1)}}{\partial \theta} + \frac{\partial N_{x\theta}^{(1)}}{\partial x} + \frac{2\sin\lambda}{r_1} N_{x\theta}^{(1)} + \frac{Q_{\theta z}^{(1)}}{r_1}\cos\lambda + \frac{r_2}{h_2 r_1} Q_{\theta z}^{(2)} - I_0^{(1)}\frac{\partial^2 v_1}{\partial t^2} - \frac{r_2}{r_1}\left(\frac{I_0^{(2)}}{2}\frac{\partial^2 v_2}{\partial t^2} - \frac{I_2^{(2)}}{h_2}\frac{\partial^2 \psi_2}{\partial t^2} \right) = 0, \\
&\frac{\partial M_{xx}^{(1)}}{\partial x} + \frac{\sin\lambda}{r_1}\left(M_{xx}^{(1)} - M_{\theta\theta}^{(1)} \right) + \frac{1}{r_1}\frac{\partial M_{x\theta}^{(1)}}{\partial \theta} - Q_{xz}^{(1)} + \frac{h_1 r_2}{2h_2 r_1} Q_{xz}^{(2)} - I_2^{(1)}\frac{\partial^2 \varphi_1}{\partial t^2} - \frac{h_1 r_2}{2r_1}\left(\frac{I_0^{(2)}}{2}\frac{\partial^2 u_2}{\partial t^2} - \frac{I_2^{(2)}}{h_2}\frac{\partial^2 \varphi_2}{\partial t^2} \right) = 0, \\
&\frac{1}{r_1}\frac{\partial M_{\theta\theta}^{(1)}}{\partial \theta} + \frac{\partial M_{x\theta}^{(1)}}{\partial x} + \frac{2\sin\lambda}{r_1} M_{x\theta}^{(1)} - Q_{\theta z}^{(1)} + \frac{h_1 r_2}{2h_2 r_1} Q_{\theta z}^{(2)} - I_2^{(1)}\frac{\partial^2 \psi_1}{\partial t^2} - \frac{h_1 r_2}{2r_1}\left(\frac{I_0^{(2)}}{2}\frac{\partial^2 v_2}{\partial t^2} - \frac{I_2^{(2)}}{h_2}\frac{\partial^2 \psi_2}{\partial t^2} \right) = 0, \\
&\frac{\partial N_{xx}^{(3)}}{\partial x} + \frac{\sin\lambda}{r_3}\left(N_{xx}^{(3)} - N_{\theta\theta}^{(3)} \right) + \frac{1}{r_3}\frac{\partial N_{x\theta}^{(3)}}{\partial \theta} - \frac{r_2}{r_3}\frac{Q_{xz}^{(2)}}{h_2} - I_0^{(3)}\frac{\partial^2 u_3}{\partial t^2} - \frac{r_2}{r_3}\left(\frac{I_0^{(2)}}{2}\frac{\partial^2 u_2}{\partial t^2} + \frac{I_2^{(2)}}{h_2}\frac{\partial^2 \varphi_2}{\partial t^2} \right) = 0, \\
&\frac{1}{r_3}\frac{\partial N_{\theta\theta}^{(3)}}{\partial \theta} + \frac{\partial N_{x\theta}^{(3)}}{\partial x} + \frac{2\sin\lambda}{r_3} N_{x\theta}^{(3)} + \frac{\cos\lambda}{r_3} Q_{\theta z}^{(3)} - \frac{r_2}{h_2 r_3} Q_{\theta z}^{(2)} - I_0^{(3)}\frac{\partial^2 v_3}{\partial t^2} - \frac{r_2}{r_3}\left(\frac{I_0^{(2)}}{2}\frac{\partial^2 v_2}{\partial t^2} + \frac{I_2^{(2)}}{h_2}\frac{\partial^2 \psi_2}{\partial t^2} \right) = 0, \\
&\frac{\partial M_{xx}^{(3)}}{\partial x} + \frac{\sin\lambda}{r_2}\left(M_{xx}^{(3)} - M_{\theta\theta}^{(3)} \right) + \frac{1}{r_3}\frac{\partial M_{x\theta}^{(3)}}{\partial \theta} - Q_{xz}^{(3)} + \frac{h_3 r_2}{2h_2 r_3} Q_{xz}^{(2)} - I_2^{(3)}\frac{\partial^2 \varphi_3}{\partial t^2} + \frac{h_3 r_2}{2r_3}\left(\frac{I_0^{(2)}}{2}\frac{\partial^2 u_2}{\partial t^2} + \frac{I_2^{(2)}}{h_2}\frac{\partial^2 \varphi_2}{\partial t^2} \right) = 0, \\
&\frac{1}{r_3}\frac{\partial M_{\theta\theta}^{(3)}}{\partial \theta} + \frac{\partial M_{x\theta}^{(3)}}{\partial x} + \frac{2\sin\lambda}{r_3} M_{x\theta}^{(3)} - Q_{\theta z}^{(3)} + \frac{h_3 r_2}{2h_2 r_3} Q_{\theta z}^{(2)} - I_2^{(3)}\frac{\partial^2 \psi_3}{\partial t^2} + \frac{h_3 r_2}{2r_3}\left(\frac{I_0^{(2)}}{2}\frac{\partial^2 v_2}{\partial t^2} + \frac{I_2^{(2)}}{h_2}\frac{\partial^2 \psi_2}{\partial t^2} \right) = 0, \\
&\frac{\partial Q_{xz}}{\partial x} + \frac{1}{r_2}\frac{\partial Q_{\theta z}}{\partial \theta} + \frac{\sin\lambda}{r_2} Q_{xz} - \frac{\cos\lambda}{r_2}\left(N_{\theta\theta}^{(1)} + N_{\theta\theta}^{(3)} \right) - \left(\frac{r_1}{r_2} I_0^{(1)} + I_0^{(2)} + \frac{r_3}{r_2} I_0^{(3)} \right)\frac{\partial^2 w}{\partial t^2} = 0.
\end{aligned} \tag{26}$$

Also, the boundary conditions at both ends of the shell (*x=0* & *L*) can be attained as described in Eqns. (27.a)-(27.c):

Clamped (C):

$$u_1 = 0, \quad v_1 = 0, \quad \varphi_1 = 0, \quad \psi_1 = 0, \quad u_3 = 0, \quad v_3 = 0, \quad \varphi_3 = 0, \quad \psi_3 = 0, \quad w = 0. \tag{27.a}$$

Simply Supported (S):

$$N_{xx}^{(1)} = 0, \quad v_1 = 0, \quad M_{xx}^{(1)} = 0, \quad \psi_1 = 0, \quad N_{xx}^{(3)} = 0, \quad v_3 = 0, \quad M_{xx}^{(3)} = 0, \quad \psi_3 = 0, \quad w = 0. \tag{27.b}$$

Free (F):

$$N_{xx}^{(1)} = 0, \quad N_{x\theta}^{(1)} = 0, \quad M_{xx}^{(1)} = 0, \quad M_{x\theta}^{(1)} = 0, \quad N_{xx}^{(3)} = 0, \quad N_{x\theta}^{(3)} = 0, \quad M_{xx}^{(3)} = 0, \quad M_{x\theta}^{(3)} = 0, \quad Q_{xz} = 0. \tag{27.c}$$

3 SOLUTION

3.1 Analytical solution in the circumferential direction

Owing to the continuity of all geometrical and physical parameters at θ=0 and 2π, the following exact solution can be considered the circumferential direction [39, 40]:

$$\begin{Bmatrix} u_i(x,\theta,t) \\ v_i(x,\theta,t) \\ \varphi_i(x,\theta,t) \\ \psi_i(x,\theta,t) \\ w(x,\theta,t) \end{Bmatrix} = \sum_{n=0}^{\infty} \begin{Bmatrix} U_{in}(x)\cos(n\theta) \\ V_{in}(x)\sin(n\theta) \\ X_{in}(x)\cos(n\theta) \\ \Theta_{in}(x)\sin(n\theta) \\ W_n(x)\cos(n\theta) \end{Bmatrix} \exp(j\Omega t), \quad i=1,3 \tag{28}$$

in which Ω is a complex eigenvalue and n is known as the circumferential wave number. By substituting Eqn. (24) into Eqn. (26) and considering the solution presented in Eqn. (28), the governing equations can be obtained which are presented in Appendix A.

By substituting Eqn. (24) into Eqn. (27.a)-(27.c) and considering the solution presented in Eqn. (28), the boundary conditions can be obtained which are presented in Appendix B.

3.2 Approximate solution in the meridional direction

In this section, the DQM is hired as a numerical method to present an approximate solution for the governing equations (A.1) under any combinations of the boundary conditions described in Eqns. (B.1)-(B.3).

According to the main idea in the DQM, each derivative of a function like $f(x)$ can be estimated in terms of the weighted sum of its values at a set of N discrete points as [41]

$$\left\{\frac{d^k f}{dx^k}\right\}_{N\times 1} = \left[A^{(k)}\right]_{N\times N}\{f\}_{N\times 1}, \tag{29}$$

in which $[A^{(k)}]$ is the weighting coefficient matrix associated with the kth-order derivative. For the first-order derivative (k=1) and the higher-order ones (k=2,3,…), this matrix can be calculated through the following relation [41]:

$$\left[A_{ij}^{(1)}\right] = \begin{cases} \dfrac{\prod\limits_{\substack{p=1 \\ p\neq i,j}}^{N}\left(x_i - x_p\right)}{\prod\limits_{\substack{p=1 \\ p\neq j}}^{N}\left(x_j - x_p\right)}, & i\neq j, \\ \sum\limits_{\substack{p=1 \\ p\neq i}}^{N}\dfrac{1}{x_i - x_p}, & i=j, \end{cases} \quad i,j=1,2,...,N. \tag{30}$$

$$\left[A^{(k)}\right] = \left[A^{(1)}\right]\left[A^{(k-1)}\right], \quad k=2,3,4,\ldots$$

The distribution pattern of the grid points has an undeniable role in the convergence rate of the solution provided by the DQM. In this paper, the Gauss–Lobatto–Chebyshev distribution pattern is used which is presented as follows [41]:

$$x_i = \left[1-\cos\left(\pi\frac{i-1}{N-1}\right)\right]\frac{L}{2}, \; i=1,2,...,N. \tag{31}$$

By applying Eqn. (29), the governing equations (A.1) can be presented in the algebraic form below:

$$[K]\{y\} = \Omega^2[M]\{y\}, \tag{32}$$

where $\{y\}$ is the displacement vector, and $[K]$ and $[M]$ are stiffness and mass matrices, respectively.

By applying Eqns. (29), any combinations of the boundary conditions (B.1)-(B.3) at x=0 & L can be presented in the algebraic form below:

$$[\Gamma]\{y\}=\{0\}. \tag{33}$$

Simultaneous solutions of the algebraic equations (32) and (33) provide complex eigenvalues Ω (More details can be found in Refs. [42, 43]). The natural frequencies of the shell (Λ) and the corresponding loss factors (ζ) can be extracted through the following relation [26]:

$$\Lambda_{nm}=\sqrt{\mathrm{Re}\left(\Omega_{nm}^{2}\right)},\quad \zeta_{nm}=\mathrm{Im}\left(\Omega_{nm}^{2}\right)\big/\mathrm{Re}\left(\Omega_{nm}^{2}\right). \tag{34}$$

As shown in Eqn. (34), vibrational modes are specified by two indices. The first one (n) is the circumferential wave number defined in Eqn. (28), and the second one (m) is used to indicate the sequence of vibrational modes in the meridional direction. The dimensionless frequency parameter is defined as follows:

$$\omega_{nm}=\Lambda_{nm}a\sqrt{\rho_0/E_0}. \tag{35}$$

4. NUMERICAL RESULTS

Numerical results and physical explanations are presented in this section. Two capital letters are used to describe the boundary conditions which show the condition at x=0 and x=L, respectively. Except for the cases which are mentioned otherwise, the results are presented for a CS shell of a=0.5 m, λ=30°, L/a=2, h_2/a=0.1, and h_1/a=h_3/a=0.02. The mechanical properties of the porous face sheets are considered as E_0=60 GPa, ρ_0=2700 kg/m^3, and ν=0.25. The porosity parameter is chosen as η_1=0.6 and the distribution pattern of pores in the surfaces is considered as SI-SI. The intensities of electrical and magnetic fields are considered as E=2.5 kV/mm and B=500 G, respectively.

4.1 Convergence and verification

The influences of the number of grid points in the numerical solution presented via the DQM on the natural frequencies and loss factors are investigated in Figure 3 for n=4 and m=1,2,3,4. As this figure shows, the presented numerical solution via the DQM benefits from a high convergence rate. In what follows, all numerical results are reported utilizing N=13 points.

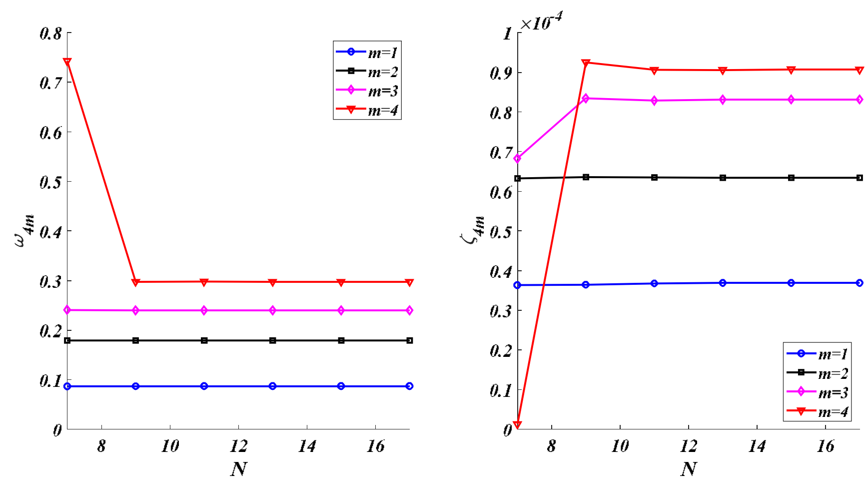

Fig. 3
Convergence analysis of the presented numerical solution via the DQM.

Two numerical examples are presented in this section to check the accuracy of the present work. As the first one, consider an SS cylindrical (λ=0) sandwich shell with an ERF core and two face sheets made of aluminum (E=70 GPa, ρ=2700 kg/m^3, ν=0.3). The geometric characteristics of the shell are selected as L=0.3 m, h_3=0.75 mm, h_1=0.2h_3, and h_2=0.5h_3. For two values of length-to-radius ratio (L/a) and several values of intensity of the electric field, the natural frequencies of the shell are tabulated in Hz in Table 2 for n=m=1 against those reported by Hasheminejad et al. [25]. As observed, the results are in high agreement which proves the accuracy of the present work.

Table 2
The natural frequencies (Hz) of an SS cylindrical shell with ERF core and isotropic homogenous face sheets (L=0.3 m, h_3=0.75 mm, h_1=0.2h_3, h_2=0.5h_3, E=70 GPa, ρ=2700 kg/m^3, ν=0.3, n=m=1)

	L/a=1		L/a=1.5	
E_e (kV/mm)	Present	Hasheminejad et al. [25]	Present	Hasheminejad et al. [25]
0.6	1461	1461	2125	2114
0.8	1464	1462	2150	2140
1.0	1470	1463	2169	2159
1.2	1474	1465	2184	2174
1.4	1478	1468	2195	2186
1.6	1480	1473	2203	2194
1.8	1482	1474	2209	2205
2.0	1483	1478	2213	2205
2.2	1484	1479	2216	2208
2.4	1485	1480	2219	2210

As the second verification example, consider a single-layer isotropic homogeneous truncated conical shell of elastic modulus E, density ρ, and Poisson's ratio ν=0.3. The geometrical factors of the shell are selected as λ=45° and $L\sin\lambda/b$=0.5, and h/b=0.01. For n=0,1,2,…,9 and m=1, the dimensionless frequency parameter defined as

$$\kappa_{nm} = \Lambda_{nm} b\sqrt{\rho\left(1-\nu^2\right)/E}, \tag{36}$$

are tabulated in Table 3 for two selected boundary conditions along with those predicted by Liew et al. [44]. As shown in this table, the results are in high agreement which proves the accuracy of the present work.

Table 3
The dimensionless frequency parameters of a single-layer isotropic homogeneous truncated conical shell (ν=0.3, λ=45° ، $L\sin\lambda/b$=0.5, h/b=0.01, m=1)

	CC		SS	
n	Present	Liew et al. [44]	Present	Liew et al. [44]
0	0.8726	0.8732	0.2230	0.2234
1	0.8117	0.8120	0.5460	0.5462
2	0.6694	0.6696	0.6308	0.6310
3	0.5426	0.5428	0.5062	0.5065
4	0.4563	0.4565	0.3942	0.3947
5	0.4085	0.4088	0.3339	0.3337
6	0.3957	0.3961	0.3236	0.3235
7	0.4134	0.4141	0.3508	0.3510
8	0.4556	0.4567	0.4015	0.4019
9	0.5160	0.5175	0.4663	0.4671

4.2. Parametric study

A parametric study is presented in this section to examine the influences of several parameters on the dimensionless frequency parameters and loss factors. Figure 4 is presented to examine the variations of the dimensionless frequency parameters and loss factors of the shell versus the variation of the circumferential wave number in different meridional mode numbers (m=1,2,3,4). As observed, the lowest dimensionless frequency parameters are not necessarily associated with the lowest value of the circumferential wave number (n=0). As the circumferential wave number increases from zero to higher values, the dimensionless frequency parameters experience an initial reduction followed by a steadily increase. This figure reveals that there is a specific value of the circumferential wave number which is associated with the highest loss factors of the shell. In this vibrational mode, the oscillations of the shell damp as quickly as possible.

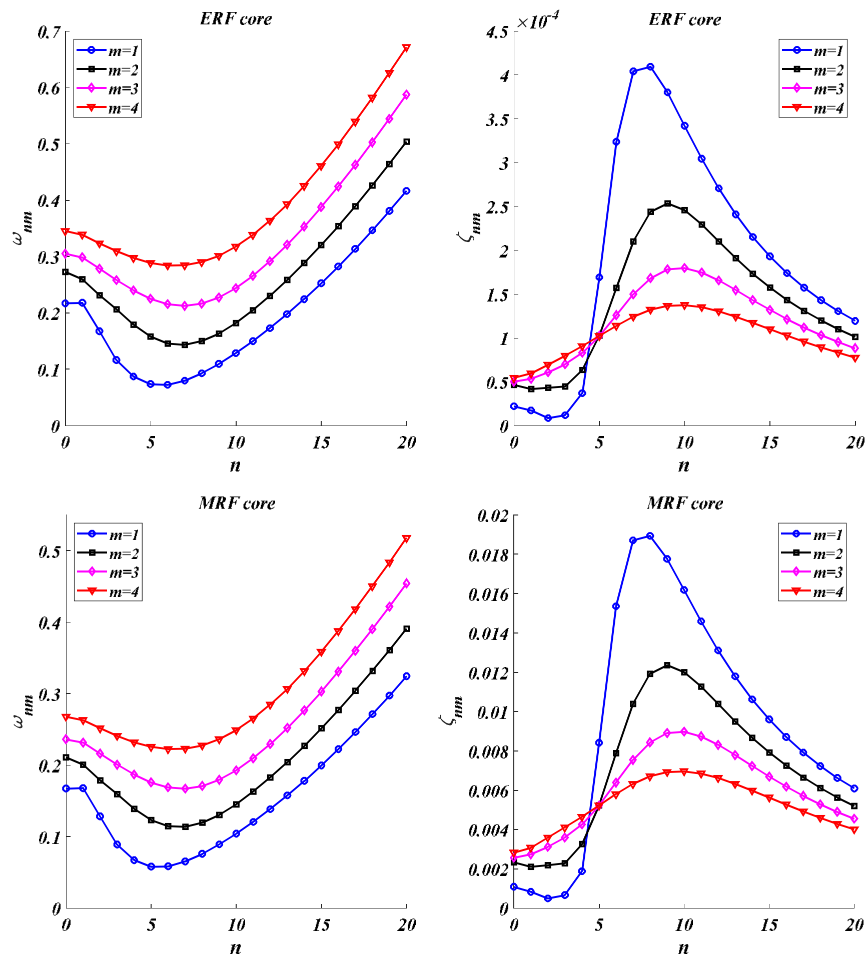

Fig. 4
The variations of the dimensionless frequency parameters and loss factors of the shell versus the variation of the circumferential wave number.

According to Figure 4, it can be concluded that the sandwich shell with ERF core benefits from higher dimensionless frequency parameters rather than the sandwich shell with MRF core. However, the sandwich shell with MRF core benefits from higher loss factors rather than the sandwich shell with ERF core. It reveals that the ERF core provides higher stiffness and the MRF core brings about a higher damping effect.

Figure 4 shows that in this case of study, for both shells with ERF and MRF cores, the four lowest dimensionless frequency parameters of the shell are associated with (n,m)=(4,1), (n,m)=(5,1), (n,m)=(6,1), and (n,m)=(7,1). In what follows, all numerical examples are reported for these four vibrational modes.

Figure 5 shows the effects of the intensities of the electric and magnetic fields on the natural frequencies and loss factors of the shell. This figure shows that for both shells with ERF and MRF cores, the dimensionless frequency parameters increase by enhancing the intensity of the field. It can be explained by the improvement in the stiffness of the rheological core. As the intensity of the field applied to the rheological core increases, more percentages of the micro-particles suspended inside the rheological fluid join to the chains consisting of micro-particles.

It is noteworthy that since most stiffness of the shell comes from the stiffness of the porous face sheets, the improvement in the stiffness of the core has a weak effect on the dimensionless frequency parameters and loss factors of the shell. Thus, to make it easier to show the corresponding variations, the ratios between the dimensionless frequency parameters and loss factors and the corresponding ones associated with E=0 and B=0 (no field) are presented in Figure 5. In other words, the following parameter is depicted in Figure 5:

$$\begin{aligned}
&\text{ERF core:}\quad \omega_{nm}^{*}=\frac{\omega_{nm}}{\left.\omega_{nm}\right|_{E=0}},\quad \zeta_{nm}^{*}=\frac{\zeta_{nm}}{\left.\zeta_{nm}\right|_{E=0}}.\\
&\text{MRF core:}\quad \omega_{nm}^{*}=\frac{\omega_{nm}}{\left.\omega_{nm}\right|_{B=0}},\quad \zeta_{nm}^{*}=\frac{\zeta_{nm}}{\left.\zeta_{nm}\right|_{B=0}}.
\end{aligned} \tag{37}$$

An increase in the intensity of the field provides higher damping of the rheological fluid. However, it does not necessarily result in higher loss factors due to the simultaneous increase in the stiffness of the rheological fluid. Thus, as Figure 5 shows, as the intensity of the electric field increases, the loss factors of the shell with ERF core decrease, and as the intensity of the magnetic field increases, the loss factors of the shell with MRF core experience an initial increase followed by a reduction.

Figure 5 reveals that in comparison with the dimensionless frequency parameters, the loss factors are more dependent on the intensity of the field. To explain this difference, it should be noted that the stiffness of the rheological core is significantly smaller than the stiffness of the porous core. However, the whole damping of the shell comes from the rheological core.

Figure 5 shows that the dimensionless frequency parameters and loss factors of the shell with MRF core are more sensitive to the intensity of the field rather than the dimensionless frequency parameters and loss factors of the shell with ERF core. In other words, the MRF core has a stronger rheological effect rather than the ERF core.

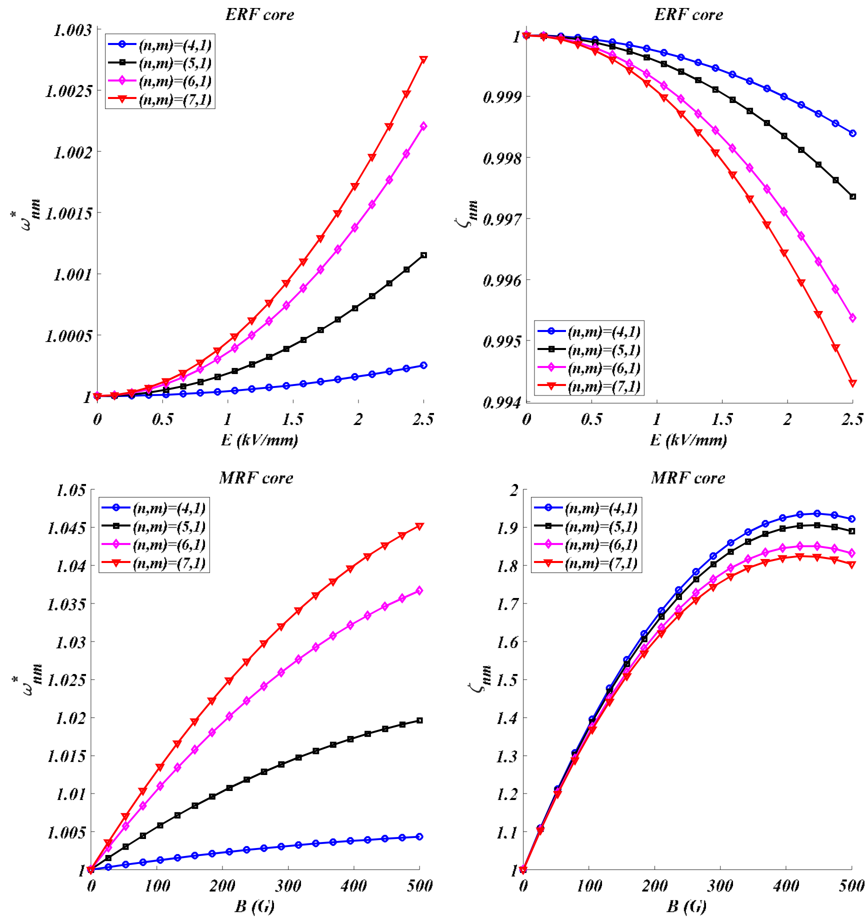

Fig. 5
The influences of the intensity of the electric and magnetic fields on the dimensionless frequency parameters and loss factors of the shell.

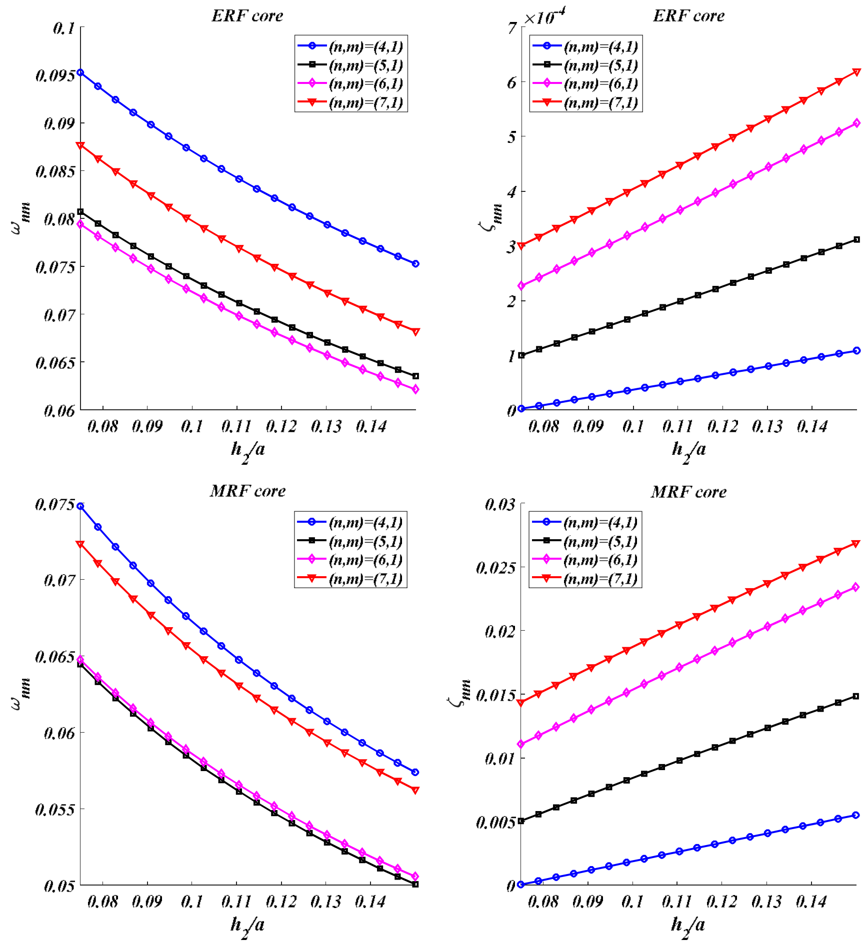

Fig. 6
The influences of thickness of the rheological core on the dimensionless frequency parameters and loss factors of the shell.

In Figure 6, the effects of the thickness of the rheological core on the dimensionless frequency parameters and loss factors are studied. The rheological core suffers from low stiffness-to-density mass. Thus, an increase in the thickness of the rheological core results in a small increase in the stiffness of the shell and a significant increase in the mass of the shell and provides lower dimensionless frequency parameters as shown in Figure 6. As stated, the whole damping behavior of the shell comes from the rheological core. Consequently, as the thickness of the rheological core increases, the loss factors of the shell grow. In other words, utilizing a thicker rheological core results in faster damping of the oscillations of the shell.

The impacts of the porosity parameter on the dimensionless frequency parameters and loss factors of the shell are examined in Figure 7. An increase in the porosity parameter decreases both the stiffness and mass of the shell. Thus, as shown in this figure, the loss factors increase by increasing the porosity parameter which is observed in Figure 7. The reductions in the stiffness and mass have opposite effects on the dimensionless frequency parameters. However, as shown in this figure, for this case of study, the rate of the reduction in the stiffness is higher than the rate of the reduction in the mass and the dimensionless frequency parameters diminish by increasing the porosity parameter.

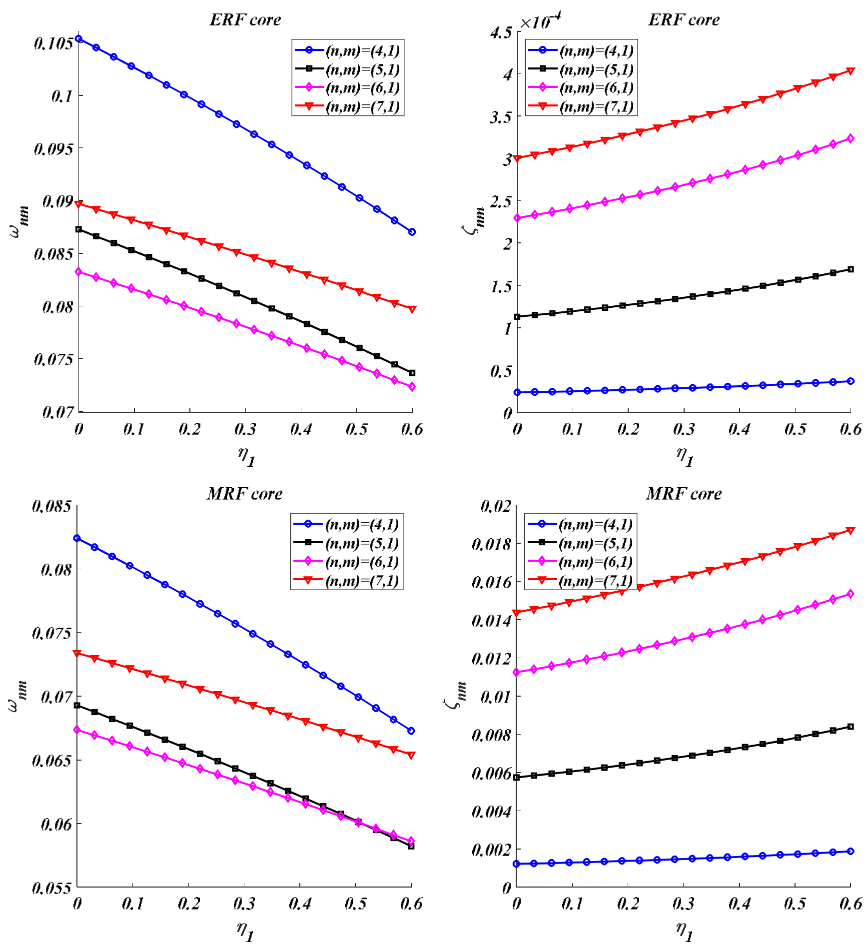

Fig. 7
The influences of the porosity parameter on the dimensionless frequency parameters and loss factors of the shell.

The impacts of the porosity distribution pattern on dimensionless frequency parameters and loss factors of the shell are examined in Table 4. As observed, in all vibrational modes and for both shells with ERF and MRF cores, the highest dimensionless frequency parameter belongs to the SI-SI porosity distribution pattern in the face sheets. The reason behind this privilege can be found in Figure 2. As this figure shows, in the SI porosity distribution pattern, larger pores are located near the neutral surface of the face sheets which results in the minimum reduction in the flexural rigidity of the face sheets. Table 4 shows that the lowest loss factors belong to the S1-S1 porosity distribution pattern, as well. The reason behind this disadvantage is the high flexural rigidity of the face sheets in this porosity distribution pattern. As a result, the key parameter is choosing the best porosity distribution pattern in the face sheets is the objective of the designer which can be either achieving the highest dimensionless frequency parameter or achieving the fastest damping of oscillations.

Table 4
The influences porosity distribution pattern on the dimensionless frequency parameters and loss factors of the shell.

		ω_{nm}			η_{nm}		
		UD-UD	SI-SI	SII-SII	UD-UD	SI-SI	SII-SII
ERF core	$(n,m)=(4,1)$	0.0844	0.0870	0.0863	0.0000	0.0000	0.0000
	$(n,m)=(5,1)$	0.0699	0.0736	0.0689	0.0002	0.0002	0.0002
	$(n,m)=(6,1)$	0.0667	0.0723	0.0621	0.0004	0.0003	0.0004
	$(n,m)=(7,1)$	0.0719	0.0797	0.0635	0.0005	0.0004	0.0007
MRF core	$(n,m)=(4,1)$	0.0653	0.0673	0.0667	0.0020	0.0019	0.0019
	$(n,m)=(5,1)$	0.0555	0.0582	0.0547	0.0093	0.0084	0.0096
	$(n,m)=(6,1)$	0.0546	0.0586	0.0513	0.0178	0.0154	0.0204
	$(n,m)=(7,1)$	0.0599	0.0654	0.0540	0.0225	0.0187	0.0280

Table 5 is devoted to investigating the effects of the boundary conditions on dimensionless frequency parameters and loss factors. As this table shows, for both shells with ERF and MRF cores and in all vibration modes, the highest dimensionless frequency parameters and the lowest loss factors belong to the CC shell, and the lowest dimensionless frequency parameters and the highest loss factors belong to the CF shell. The reasons behind these characteristics are the lowest degree of freedom in the clamped condition which results in the highest stiffness, and the highest degree of freedom in the free condition which leads to the lowest stiffness.

Comparisons between dimensionless frequency parameters for SC and CS shells or FC and CF shells reveal that SC and FC shells have higher dimensionless frequency parameters rather than CS and CF shells, respectively. It shows that the dimensionless frequency parameters are more dependent on the condition at the large radius of the shell ($x=L$) rather than the small radius of the shell ($x=0$). It can be explained by the higher perimeter of the shell at $x=L$ which brings about a larger boundary.

Table 5
The influences of the boundary conditions on the dimensionless frequency parameters and loss factors of the shell.

			CC	SS	CS	SC	CF	FC
ERF core	ω_{nm}	$(n,m)=(4,1)$	0.1024	0.0793	0.0870	0.0950	0.0242	0.0558
		$(n,m)=(5,1)$	0.0883	0.0667	0.0736	0.0815	0.0278	0.0582
		$(n,m)=(6,1)$	0.0849	0.0679	0.0723	0.0800	0.0366	0.0698
		$(n,m)=(7,1)$	0.0902	0.0776	0.0797	0.0875	0.0483	0.0840
	η_{nm}	$(n,m)=(4,1)$	0.0000	0.0000	0.0000	0.0000	0.0002	0.0001
		$(n,m)=(5,1)$	0.0001	0.0002	0.0002	0.0002	0.0005	0.0004
		$(n,m)=(6,1)$	0.0003	0.0004	0.0003	0.0003	0.0007	0.0004
		$(n,m)=(7,1)$	0.0003	0.0004	0.0004	0.0004	0.0007	0.0004
MRF core	ω_{nm}	$(n,m)=(4,1)$	0.0792	0.0613	0.0673	0.0735	0.0178	0.0434
		$(n,m)=(5,1)$	0.0694	0.0530	0.0582	0.0643	0.0230	0.0474
		$(n,m)=(6,1)$	0.0680	0.0554	0.0586	0.0645	0.0314	0.0575
		$(n,m)=(7,1)$	0.0732	0.0639	0.0654	0.0714	0.0414	0.0691
	η_{nm}	$(n,m)=(4,1)$	0.0019	0.0021	0.0019	0.0021	0.0140	0.0041
		$(n,m)=(5,1)$	0.0067	0.0102	0.0084	0.0079	0.0200	0.0163
		$(n,m)=(6,1)$	0.0124	0.0174	0.0154	0.0140	0.0294	0.0196
		$(n,m)=(7,1)$	0.0160	0.0198	0.0187	0.0171	0.0294	0.0191

5. CONCLUSIONS

In this paper, the free vibration analysis of a truncated conical three-layered sandwich shell with either ERF or MRF core and FG porous face sheets was studied. The FSDT was utilized to perform the mathematical modeling of the layers of the shell incorporating the continuity conditions between the layers. Three porosity distribution patterns were considered for the face sheets including a uniform one and two FG non-uniform ones. The influences of various factors on the dimensionless frequency parameters and loss factors were examined. The main findings and achievements of the present work can be stated as follows:

- The sandwich shell with ERF core benefits from higher dimensionless frequency parameters rather than the sandwich shell with MRF core.
- The sandwich shell with MRF core benefits from higher loss factors rather than the sandwich shell with ERF core.
- The dimensionless frequency parameters increase by increasing the intensity of the electric and magnetic fields.
- An eenhancement in the intensity of the electric and magnetic fields does not necessarily provide higher loss factors.
- In comparison with the dimensionless frequency parameters, the loss factors are more sensitive to the variations in the intensity of the electric and magnetic fields.
- The dimensionless frequency parameters and loss factors of the shell with the MRF core are more dependent on the intensity of the field rather than the dimensionless frequency parameters and loss factors of the shell with the ERF core.
- An increase in the thickness of the rheological core results in lower dimensionless frequency parameters and higher loss factors.
- An increase in the porosity parameter provides lower dimensionless frequency parameters and higher loss factors.
- The highest dimensionless frequency parameters and the lowest loss factors can be attained when the pores are located near the neutral surfaces of the face sheets.
- Utilizing the boundary conditions with lower degrees of freedom (clamped) results in higher dimensionless frequency parameters.
- Utilizing the boundary conditions with higher degrees of freedom (free) results in higher loss factors.
- The dimensionless frequency parameters are more sensitive to the condition at the large radius of the shell rather than its small radius.

REFERENCES

[1] A. Ghorbanpour Arani, A. Rastgoo, M. Sharafi, R. Kolahchi, A. Ghorbanpour Arani, Nonlocal viscoelasticity based vibration of double viscoelastic piezoelectric nanobeam systems, Meccanica 51 (2016) 25-40.
[2] A. Ghorbanpour Arani, A. Rastgoo, A. Hafizi Bidgoli, R. Kolahchi, A. Ghorbanpour Arani, Wave propagation of coupled double-DWBNNTs conveying fluid-systems using different nonlocal surface piezoelasticity theories, Mechanics of Advanced Materials and Structures 24(14) (2017) 1159-1179.
[3] P. Sourani, A. Ghorbanpour Arani, M. Hashemian, S. Niknejad, Nonlinear dynamic stability analysis of CNTs reinforced piezoelectric viscoelastic composite nano/micro plate under multiple physical fields resting on smart foundation, Proceedings of the Institution of Mechanical Engineers, Part C: Journal of Mechanical Engineering Science 238(10) (2024) 4307-4342.
[4] A. Ghorbanpour Arani, M. Abdollahian, A. Ghorbanpour Arani, Nonlinear dynamic analysis of temperature-dependent functionally graded magnetostrictive sandwich nanobeams using different beam theories, Journal of the Brazilian Society of Mechanical Sciences and Engineering 42 (2020) 1-20.
[5] A. Ghorbanpour Arani, Z.K. Maraghi, A. Ghorbanpour Arani, The Frequency Response of Intelligent Composite Sandwich Plate Under Biaxial In-Plane Forces, Journal of Solid Mechanics 15(1) (2023).
[6] A. Ghorbanpour Arani, N. Miralaei, A. Farazin, M. Mohammadimehr, An extensive review of the repair behavior of smart self-healing polymer matrix composites, Journal of Materials Research 38(3) (2023) 617-632.
[7] M. Alinejad, S. Jafari Mehrabadi, M.M. Najafizadeh, Free vibration analysis of a porous functionally graded, truncated conical shell with a magneto-rheological fluid core, Mechanics of Advanced Materials and Structures 31(5) (2024) 1006-1020.
[8] M. Alinejad, S. Jafari Mehradadi, M.M. Najafizadeh, Free vibration analysis of a sandwich conical shell with a magnetorheological elastomer core, enriched with carbone nanotubes and functionally graded porous face layers, Noise & Vibration Worldwide (2024) 09574565241252993.
[9] S. Nagiredla, S. Joladarashi, H. Kumar, Experimental investigation of frequency and damping characteristics of magneto-rheological fluid core sandwich beams, AIP Conference Proceedings, AIP Publishing, 2020.
[10] N. Srinivasa, T. Gurubasavaraju, H. Kumar, M. Arun, Vibration analysis of fully and partially filled sandwiched cantilever beam with Magnetorheological fluid, J. Eng. Sci. Technol 15 (2020) 3162-3177.

[11] M. Eshaghi, The effect of magnetorheological fluid and aerodynamic damping on the flutter boundaries of MR fluid sandwich plates in supersonic airflow, European Journal of Mechanics-A/Solids 82 (2020) 103997.
[12] M. Eshaghi, Supersonic flutter analysis of annular/circular sandwich panels containing magnetorheological fluid, Journal of Sandwich Structures & Materials 23(7) (2021) 2968-2987.
[13] A. Ghorbanpour Arani, A. Rastgoo, Vibration Analysis of the Sandwich Beam with Electro-Rheological Fluid Core Embedded Within Two FG Nanocomposite Faces Resting on Pasternak Foundation, Journal of Solid Mechanics 12(4) (2020).
[14] A. Ghorbanpour Arani, S. Jamali, The vibration of the cylindrically curved sandwich plate with rheological core and nanocomposite face sheets rested on the Winkler–Pasternak foundation, Journal of Sandwich Structures & Materials 23(6) (2021) 2196-2216.
[15] M. Gholamzadeh Babaki, M. Shakouri, Free and forced vibration of sandwich plates with electrorheological core and functionally graded face layers, Mechanics Based Design of Structures and Machines 49(5) (2021) 689-706.
[16] R. Aboutalebi, M. Eshaghi, A. Taghvaeipour, Nonlinear vibration analysis of circular/annular/sector sandwich panels incorporating magnetorheological fluid operating in the post-yield region, Journal of Intelligent Material Systems and Structures 32(7) (2021) 781-796.
[17] A.O. Soroor, M. Asgari, H. Haddadpour, Effect of axially graded constraining layer on the free vibration properties of three layered sandwich beams with magnetorheological fluid core, Composite Structures 255 (2021) 112899.
[18] F. Ebrahimi, S.B. Sedighi, Wave propagation analysis of a rectangular sandwich composite plate with tunable magneto-rheological fluid core, Journal of Vibration and Control 27(11-12) (2021) 1231-1239.
[19] M. Keshavarzian, M.M. Najafizadeh, K. Khorshidi, P. Yousefi, S.M. Alavi, Comparison of the application of smart electrorheological and magnetorheological fluid cores to damp sandwich panels' vibration behavior, based on a novel higher-order shear deformation theory, Proceedings of the Institution of Mechanical Engineers, Part E: Journal of Process Mechanical Engineering 236(2) (2022) 225-244.
[20] M. Keshavarzian, M.M. Najafizadeh, K. Khorshidi, P. Yousefi, S.M. Alavi, Non-linear free vibration analysis of a thick sandwich panel with an electrorheological core, Journal of Vibration Engineering & Technologies 10(4) (2022) 1495-1509.
[21] P. Shahali, H. Haddadpour, S. Shakhesi, Dynamic analysis of electrorheological fluid sandwich cylindrical shells with functionally graded face sheets using a semi-analytical approach, Composite Structures 295 (2022) 115715.
[22] A. Shariati, S.S. Bayrami, F. Ebrahimi, A. Toghroli, Wave propagation analysis of electro-rheological fluid-filled sandwich composite beam, Mechanics Based Design of Structures and Machines 50(5) (2022) 1481-1490.
[23] K. Khorshidi, B. Soltannia, M. Karimi, A. Ghorbani, Nonlinear vibration of electro-rheological sandwich plates, coupled to quiescent fluid, Ocean Engineering 271 (2023) 113730.
[24] S.M. Farahani, S. Jafari Mehrabadi, S.V. Mohammadi, Vibration analysis of a smart viscoelastic porous sandwich micro-shell with magnetorheological fluid core using the modified couple stress theory, Waves in Random and Complex Media (2024) 1-31.
[25] S.M. Hasheminejad, M.A. Motaaleghi, Supersonic flutter control of an electrorheological fluid-based smart circular cylindrical shell, International Journal of Structural Stability and Dynamics 14(02) (2014) 1350064.
[26] P. Cupial, J. Niziol, Vibration and damping analysis of a three-layered composite plate with a viscoelastic mid-layer, Journal of Sound and Vibration 183(1) (1995) 99-114.
[27] R. Selvaraj, M. Ramamoorthy, A.B. Arumugam, Experimental and numerical studies on dynamic performance of the rotating composite sandwich panel with CNT reinforced MR elastomer core, Composite Structures 277 (2021) 114560.
[28] J.-Y. Yeh, Finite element analysis of the cylindrical shells subjected to ER damping treatment, Smart materials and structures 17(3) (2008) 035022.
[29] V. Rajamohan, R. Sedaghati, S. Rakheja, Vibration analysis of a multi-layer beam containing magnetorheological fluid, Smart Materials and Structures 19(1) (2009) 015013.
[30] H. Afshari, Free vibration analysis of GNP-reinforced truncated conical shells with different boundary conditions, Australian Journal of Mechanical Engineering 20(5) (2022) 1363-1378.
[31] H. Amirabadi, A. Mottaghi, M. Sarafraz, H. Afshari, Free vibrational behavior of a conical sandwich shell with a functionally graded auxetic honeycomb core, Journal of Vibration and Control (2024) 10775463241240215.
[32] H. Afshari, Y. Ariaseresht, S.S. Rahimian Koloor, H. Amirabadi, M.O. Bidgoli, Supersonic flutter behavior of a polymeric truncated conical shell reinforced with agglomerated CNTs, Waves in Random and Complex Media (2022) 1-25.
[33] V. Mohammadlou, Z. Khoddami Maraghi, A. Ghorbanpour Arani, Thermoelastic analysis of axisymmetric conical shells: Investigating stress–strain response under uniform heat flow with semi-coupled approach, Numerical Heat Transfer, Part A: Applications (2024) 1-22.
[34] J.N. Reddy, Mechanics of laminated composite plates and shells: theory and analysis, CRC press2003.
[35] A. Ghorbanpour Arani, M. Jamali, A. Ghorbanpour-Arani, R. Kolahchi, M. Mosayyebi, Electro-magneto wave propagation analysis of viscoelastic sandwich nanoplates considering surface effects, Proceedings of the Institution of Mechanical Engineers, Part C: Journal of Mechanical Engineering Science 231(2) (2017) 387-403.
[36] J.N. Reddy, Energy principles and variational methods in applied mechanics, John Wiley & Sons2017.
[37] A. Ghorbanpour Arani, E. Haghparast, A. Ghorbanpour Arani, Size□dependent vibration of double□bonded carbon nanotube□reinforced composite microtubes conveying fluid under longitudinal magnetic field, Polymer Composites 37(5) (2016) 1375-1383.
[38] E. Haghparast, A. Ghorbanpour Arani, A.G. Arani, Effect of fluid–structure interaction on vibration of moving sandwich plate with Balsa wood core and nanocomposite face sheets, International Journal of Applied Mechanics 12(07) (2020) 2050078.

[39] H. Afshari, Effect of graphene nanoplatelet reinforcements on the dynamics of rotating truncated conical shells, Journal of the Brazilian Society of Mechanical Sciences and Engineering 42(10) (2020) 1-22.
[40] H. Afshari, H. Amirabadi, Vibration characteristics of rotating truncated conical shells reinforced with agglomerated carbon nanotubes, Journal of Vibration and Control 28(15-16) (2022) 1894-1914.
[41] C.W. Bert, M. Malik, Differential quadrature method in computational mechanics: a review, (1996).
[42] A. Darakhsh, S. Rahmani, H. Amirabadi, M. Sarafraz, H. Afshari, Dynamics of a three-phase polymer/fiber/CNT laminated nanocomposite conical shell with nonuniform thickness, Journal of the Brazilian Society of Mechanical Sciences and Engineering 46(1) (2024) 40.
[43] M. Irani Rahaghi, A. Mohebbi, H. Afshari, Longitudinal-torsional and two plane transverse vibrations of a composite Timoshenko rotor, (2016).
[44] K.M. Liew, T.Y. Ng, X. Zhao, Free vibration analysis of conical shells via the element-free kp-Ritz method, Journal of Sound and Vibration 281(3-5) (2005) 627-645.

Appendix A

$$
\begin{aligned}
&A_{11}^{(1)}U_{1n}'' + \frac{\sin\lambda}{r_1}A_{11}^{(1)}U_{1n}' - \left[\frac{1}{r_1^2}\left(A_{22}^{(1)}\sin^2\lambda + n^2A_{66}^{(1)}\right) + \frac{r_2}{r_1}\frac{G_c}{h_2}\right]U_{1n} + \frac{n}{r_1}\left(A_{12}^{(1)} + A_{66}^{(1)}\right)V_{1n}' - \frac{n\sin\lambda}{r_1^2}\left(A_{22}^{(1)} + A_{66}^{(1)}\right)V_{1n} \\
&-\frac{r_2}{r_1}\frac{h_1}{2h_2}G_2^{*}X_{1n} + \frac{r_2}{r_1}\frac{G_c}{h_2}U_{3n} - \frac{r_2}{r_1}\frac{h_3}{2h_2}G_cX_{3n} + \left(\frac{\cos\lambda}{r_1}A_{12}^{(1)} + \frac{r_2}{r_1}G_c\right)W_n' - \frac{\sin 2\lambda}{2r_1^2}A_{22}^{(1)}W_n \\
&= \Omega^2\left[-\left(I_0^{(1)} + \frac{r_2}{r_1}q^{(2)}\right)U_{1n} - \frac{r_2}{r_1}\frac{h_1}{2}q^{(2)}X_{1n} - \frac{r_2}{r_1}p^{(2)}U_{3n} + \frac{r_2}{r_1}\frac{h_3}{2}p^{(2)}X_{3n}\right], \\
&-\frac{n}{r_1}\left(A_{12}^{(1)} + A_{66}^{(1)}\right)U_{1n}' - \frac{n\sin\lambda}{r_1^2}\left(A_{22}^{(1)} + A_{66}^{(1)}\right)U_{1n} + A_{66}^{(1)}V_{1n}'' + \frac{\sin\lambda}{r_1}A_{66}^{(1)}V_{1n}' - \left[\frac{1}{r_1^2}\left(n^2A_{22}^{(1)} + A_{44}^{(1)}\cos^2\lambda + A_{66}^{(1)}\sin^2\lambda\right) + \frac{r_2}{r_1}\frac{G_c}{h_2}\right]V_{1n} \\
&+\left(\frac{\cos\lambda}{r_1}A_{44}^{(1)} - \frac{r_2}{r_1}\frac{h_1}{2h_2}G_c\right)\Theta_{1n} + \frac{r_2}{r_1}\frac{G_c}{h_2}V_{3n} - \frac{r_2}{r_1}\frac{h_3}{2h_2}G_c\Theta_{3n} - n\left[\frac{\cos\lambda}{r_1^2}\left(A_{22}^{(1)} + A_{44}^{(1)}\right) + \frac{r_2}{r_1}\frac{G_c}{r_1}\right]W_n \\
&= \Omega^2\left[-\left(I_0^{(1)} + \frac{r_2}{r_1}q^{(2)}\right)V_{1n} - \frac{r_2}{r_1}\frac{h_1}{2}q^{(2)}\Theta_{1n} - \frac{r_2}{r_1}p^{(2)}V_{3n} + \frac{r_2}{r_1}\frac{h_3}{2}p^{(2)}\Theta_{3n}\right], \\
&-\frac{r_2}{r_1}\frac{h_1}{2h_2}G_cU_{1n} + D_{11}^{(1)}X_{1n}'' + \frac{\sin\lambda}{r_1}D_{11}^{(1)}X_{1n}' - \left[A_{55}^{(1)} + \frac{r_2}{r_1}\frac{h_1^2}{4h_2}G_c + \frac{1}{r_1^2}\left(D_{22}^{(1)}\sin^2\lambda + n^2D_{66}^{(1)}\right)\right]X_{1n} + \frac{n}{r_1}\left(D_{12}^{(1)} + D_{66}^{(1)}\right)\Theta_{1n}' \\
&-\frac{n\sin\lambda}{r_1^2}\left(D_{22}^{(1)} + D_{66}^{(1)}\right)\Theta_{1n} + \frac{r_2}{r_1}\frac{h_1}{2h_2}G_cU_{3n} - \frac{r_2}{r_1}\frac{h_1h_3}{4h_2}G_cX_{3n} - \left(A_{55}^{(1)} - \frac{r_2}{r_1}\frac{h_1}{2}G_c\right)W_n' \\
&= \Omega^2\left[-\frac{r_2}{r_1}\frac{h_1}{2}q^{(2)}U_{1n} - \left(I_2^{(1)} + \frac{r_2}{r_1}\frac{h_1^2}{4}q^{(2)}\right)X_{1n} - \frac{r_2}{r_1}\frac{h_1}{2}p^{(2)}U_{3n} + \frac{r_2}{r_1}\frac{h_1h_3}{4}p^{(2)}X_{3n}\right], \\
&\left(\frac{\cos\lambda}{r_1}A_{44}^{(1)} - \frac{r_2}{r_1}\frac{h_1}{2h_2}G^{*}\right)V_{1n} - \frac{n}{r_1}\left(D_{12}^{(1)} + D_{66}^{(1)}\right)X_{1n}' - \frac{n\sin\lambda}{r_1^2}\left(D_{22}^{(1)} + D_{66}^{(1)}\right)X_{1n} + D_{66}^{(1)}\Theta_{1n}'' + \frac{D_{66}^{(1)}\sin\alpha}{r_1}\Theta_{1n}' \\
&-\left[A_{44}^{(1)} + \frac{r_2}{r_1}\frac{h_1^2}{4h_2}G_c + \frac{1}{r_1^2}\left(n^2D_{22}^{(1)} + D_{66}^{(1)}\sin^2\lambda\right)\right]\Theta_{1n} + \frac{r_2}{r_1}\frac{h_1}{2h_2}G_cV_{3n} - \frac{r_2}{r_1}\frac{h_1h_3}{4h_2}G_c\Theta_{3n} + \frac{n}{r_1}\left(A_{44}^{(1)} - \frac{r_2}{r_1}\frac{h_1}{2}G_c\right)W_n \\
&= \Omega^2\left[-\frac{r_2}{r_1}\frac{h_1}{2}q^{(2)}V_{1n} - \left(I_2^{(1)} + \frac{r_2}{r_1}\frac{h_1^2}{4}q^{(2)}\right)\Theta_{1n} - \frac{r_2}{r_1}\frac{h_1}{2}p^{(2)}V_{3n} + \frac{r_2}{r_1}\frac{h_1h_3}{4}p^{(2)}\Theta_{3n}\right], \\
&\frac{r_2}{r_3}\frac{G_c}{h_2}U_{1n} + \frac{r_2}{r_3}\frac{h_1}{2h_2}G_cX_{1n} + A_{11}^{(3)}U_{3n}'' + \frac{\sin\lambda}{r_3}A_{11}^{(3)}U_{3n}' - \left[\frac{1}{r_3^2}\left(A_{22}^{(3)}\sin^2\lambda + n^2A_{66}^{(3)}\right) + \frac{r_2}{r_3}\frac{G_c}{h_2}\right]U_{3n} + \frac{n}{r_3}\left(A_{12}^{(3)} + A_{66}^{(3)}\right)V_{3n}' \\
&-\frac{n\sin\lambda}{r_3^2}\left(A_{22}^{(3)} + A_{66}^{(3)}\right)V_{3n} + \frac{r_2}{r_3}\frac{h_3}{2h_2}G_cX_{3n} + \left(\frac{\cos\lambda}{r_3}A_{12}^{(3)} - \frac{r_2}{r_3}G_c\right)W_n' - \frac{\sin 2\lambda}{2r_3^2}A_{22}^{(3)}W_n \\
&= \Omega^2\left[-\frac{r_2}{r_3}p^{(2)}U_{1n} - \frac{h_1}{2}\frac{r_2}{r_3}p^{(2)}X_{1n} - \left(I_0^{(3)} + \frac{r_2}{r_3}q^{(2)}\right)U_{3n} + \frac{r_2}{r_3}\frac{h_3}{2}q^{(2)}X_{3n}\right],
\end{aligned}
\tag{A.1}
$$

$$\frac{r_2}{r_3}\frac{G_c}{h_2}V_{1n}+\frac{r_2}{r_3}\frac{h_1}{2h_2}G_c\Theta_{1n}-\frac{n}{r_3}\left(A_{12}^{(3)}+A_{66}^{(3)}\right)U'_{3n}-\frac{n\sin\lambda}{r_3^2}\left(A_{22}^{(3)}+A_{66}^{(3)}\right)U_{3n}+A_{66}^{(3)}V''_{3n}+\frac{\sin\lambda}{r_3}A_{66}^{(3)}V'_{3n}$$
$$-\left[\frac{1}{r_3^2}\left(n^2A_{22}^{(3)}+A_{44}^{(3)}\cos^2\lambda+A_{66}^{(3)}\sin^2\lambda\right)+\frac{r_2}{r_3}\frac{G_c}{h_2}\right]V_{3n}+\left(\frac{\cos\lambda}{r_3}A_{44}^{(3)}+\frac{r_2}{r_3}\frac{h_3}{2h_2}G_c\right)\Theta_{3n}$$
$$-n\left[\frac{\cos\lambda}{r_3^2}\left(A_{22}^{(3)}+A_{44}^{(3)}\right)-\frac{r_2}{r_3}\frac{G_c}{r_3}\right]W_n=\Omega^2\left[-\frac{r_2}{r_3}p^{(2)}V_{1n}-\frac{r_2}{r_3}\frac{h_1}{2}p^{(2)}\Theta_{1n}-\left(I_0^{(3)}+\frac{r_2}{r_3}q^{(2)}\right)V_{3n}+\frac{r_2}{r_3}\frac{h_3}{2}q^{(2)}\Theta_{3n}\right],$$
$$-\frac{r_2}{r_3}\frac{h_3}{2h_2}G_cU_{1n}-\frac{r_2}{r_3}\frac{h_1h_3}{4h_2}G_cX_{1n}+\frac{r_2}{r_3}\frac{h_3}{2h_2}G_cU_{3n}+D_{11}^{(3)}X''_{3n}+\frac{\sin\lambda}{r_3}D_{11}^{(3)}X'_{3n}-\left[A_{55}^{(3)}+\frac{r_2}{r_3}\frac{h_3^2}{4h_2}G^*\right.$$
$$\left.+\frac{1}{r_3^2}\left(D_{22}^{(3)}\sin^2\lambda+n^2D_{66}^{(3)}\right)\right]X_{3n}+\frac{n}{r_3}\left(D_{12}^{(3)}+D_{66}^{(3)}\right)\Theta'_{3n}-\frac{n\sin\lambda}{r_3^2}\left(D_{22}^{(3)}+D_{66}^{(3)}\right)\Theta_{3n}-\left(A_{55}^{(3)}-\frac{r_2}{r_3}\frac{h_3}{2}G_c\right)W'_n$$
$$=\Omega^2\left[\frac{r_2}{r_3}\frac{h_3}{2}p^{(2)}U_{1n}+\frac{r_2}{r_3}\frac{h_1h_3}{4}p^{(2)}X_{1n}+\frac{r_2}{r_3}\frac{h_3}{2}q^{(2)}U_{3n}-\left(I_2^{(3)}+\frac{r_2}{r_3}\frac{h_3^2}{4}q^{(2)}\right)X_{3n}\right],$$
$$-\frac{r_2}{r_3}\frac{h_3}{2h_2}G_cV_{1n}-\frac{r_2}{r_3}\frac{h_1h_3}{4h_2}G_c\Theta_{1n}+\left(\frac{\cos\lambda}{r_3}A_{44}^{(3)}+\frac{r_2}{r_3}\frac{h_3}{2h_2}G_c\right)V_{3n}-\frac{n}{r_3}\left(D_{12}^{(3)}+D_{66}^{(3)}\right)X'_{3n}-\frac{n\sin\lambda}{r_3^2}\left(D_{22}^{(3)}+D_{66}^{(3)}\right)X_{3n}$$
$$+D_{66}^{(3)}\Theta''_{3n}+\frac{\sin\lambda}{r_3}D_{66}^{(3)}\Theta'_{3n}-\left[A_{44}^{(3)}+\frac{r_2}{r_3}\frac{h_3^2}{4h_2}G_c+\frac{1}{r_3^2}\left(n^2D_{22}^{(3)}+D_{66}^{(3)}\sin^2\lambda\right)\right]\Theta_{3n}+\frac{n}{r_3}\left(A_{44}^{(3)}-\frac{r_2}{r_3}\frac{h_3}{2}G_c\right)W_n$$
$$=\Omega^2\left[\frac{r_2}{r_3}\frac{h_3}{2}p^{(2)}V_{1n}+\frac{r_2}{r_3}\frac{h_1h_3}{4}p^{(2)}\Theta_{1n}+\frac{r_2}{r_3}\frac{h_3}{2}q^{(2)}V_{3n}-\left(I_2^{(3)}+\frac{r_2}{r_3}\frac{h_3^2}{4}q^{(2)}\right)\Theta_{3n}\right],$$
$$-\left(\frac{\cos\lambda}{r_2}A_{12}^{(1)}+G_c\right)U'_{1n}-\frac{\sin\lambda}{r_2}\left(\frac{A_{22}^{(1)}\cos\lambda}{r_1}+G_c\right)U_{1n}-\frac{n}{r_2}\left[\frac{\cos\lambda}{r_1}\left(A_{22}^{(1)}+A_{44}^{(1)}\right)+G_c\right]V_{1n}+\left(\frac{r_1}{r_2}A_{55}^{(1)}-\frac{h_1}{2}G_c\right)X'_{1n}$$
$$+\frac{\sin\lambda}{r_2}\left(\frac{r_1}{r_2}A_{55}^{(1)}-\frac{h_1}{2}G_c\right)X_{1n}+\frac{n}{r_2}\left(A_{44}^{(1)}-\frac{h_1}{2}G_c\right)\Theta_{1n}-\left(\frac{\cos\lambda}{r_2}A_{12}^{(3)}-G_c\right)U'_{3n}-\frac{\sin\lambda}{r_2}\left(\frac{A_{22}^{(3)}\cos\lambda}{r_3}-G_c\right)U_{3n}$$
$$-\frac{n}{r_2}\left[\frac{\cos\lambda}{r_3}\left(A_{22}^{(3)}+A_{44}^{(3)}\right)-G_c\right]V_{3n}+\left(\frac{r_3}{r_2}A_{55}^{(3)}-\frac{h_3}{2}G_c\right)X'_{3n}+\frac{\sin\lambda}{r_2}\left(\frac{r_3}{r_2}A_{55}^{(3)}-\frac{h_3}{2}G_c\right)X_{3n}+\frac{n}{r_2}\left(A_{44}^{(3)}-\frac{h_3}{2}G_c\right)\Theta_{3n}$$
$$+\left(\frac{r_1}{r_2}A_{55}^{(1)}+h_2G_c+\frac{r_3}{r_2}A_{55}^{(3)}\right)W''_n+\frac{\sin\lambda}{r_2}\left(\frac{r_1}{r_2}A_{55}^{(1)}+h_2G_c+\frac{r_3}{r_2}A_{55}^{(3)}\right)W'_n-\left[\frac{\cos^2\lambda}{r_2}\left(\frac{A_{22}^{(1)}}{r_1}+\frac{A_{22}^{(3)}}{r_3}\right)+\frac{n^2}{r_2}\left(\frac{A_{44}^{(1)}}{r_1}+\frac{h_2}{r_2}G_c+\frac{A_{44}^{(3)}}{r_3}\right)\right]W_n$$
$$=-\left(\frac{r_1}{r_2}I_0^{(1)}+I_0^{(2)}+\frac{r_3}{r_2}I_0^{(3)}\right)\Omega^2W_n,$$

where prime indicates derivative with respect to the spatial variable x and

$$p^{(2)}=0.25I_0^{(2)}-h_2^{-2}I_2^{(2)},\quad q^{(2)}=0.25I_0^{(2)}+h_2^{-2}I_2^{(2)}. \tag{A.2}$$

Appendix B

Clamped (C):

$$
\begin{aligned}
&U_{1n}=0, \quad V_{1n}=0, \quad X_{1n}=0,\\
&\Theta_{1n}=0, \quad U_{3n}=0, \quad V_{3n}=0,\\
&X_{3n}=0, \quad \Theta_{3n}=0, \quad W_{n}=0.
\end{aligned} \tag{B.1}
$$

Simply Supported (S):

$$
\begin{aligned}
&A_{11}^{(1)}\frac{\partial U_{1n}}{\partial x}+\frac{\sin\lambda}{r_1}A_{12}^{(1)}U_{1n}=0, \quad V_{1n}=0, \quad D_{11}^{(1)}\frac{\partial X_{1n}}{\partial x}+\frac{\sin\lambda}{r_1}D_{12}^{(1)}X_{1n}=0, \quad \Theta_{1n}=0,\\
&A_{11}^{(3)}\frac{\partial U_{3n}}{\partial x}+\frac{\sin\lambda}{r_3}A_{12}^{(3)}U_{3n}=0, \quad V_{3n}=0, \quad D_{11}^{(3)}\frac{\partial X_{3n}}{\partial x}+\frac{\sin\lambda}{r_3}D_{12}^{(3)}X_{3n}=0, \quad \Theta_{3n}=0, \quad W_{n}=0.
\end{aligned} \tag{B.2}
$$

Free (F):

$$
\begin{aligned}
&A_{11}^{(1)}U'_{1n}+\frac{\sin\lambda}{r_1}A_{12}^{(1)}U_{1n}+\frac{n}{r_1}A_{12}^{(1)}V_{1n}+\frac{\cos\lambda}{r_1}A_{12}^{(1)}W_{n}=0, \quad D_{11}^{(1)}X'_{1n}+\frac{\sin\lambda}{r_1}D_{12}^{(1)}X_{1n}+\frac{n}{r_1}D_{12}^{(1)}\Theta_{1n}=0,\\
&-\frac{n}{r_1}U_{1n}+V'_{1n}-\frac{\sin\lambda}{r_1}V_{1n}=0, \quad -\frac{n}{r_1}X_{1n}+\Theta'_{1n}-\frac{\sin\lambda}{r_1}\Theta_{1n}=0, \quad A_{11}^{(3)}U'_{3n}+\frac{\sin\lambda}{r_3}A_{12}^{(3)}U_{3n}+\frac{n}{r_3}A_{12}^{(3)}V_{3n}+\frac{\cos\lambda}{r_3}A_{12}^{(3)}W_{n} =\\
&D_{11}^{(3)}X'_{3n}+\frac{\sin\lambda}{r_3}D_{12}^{(3)}X_{3n}+\frac{n}{r_3}D_{12}^{(3)}\Theta_{3n}=0, \quad -\frac{n}{r_3}U_{3n}+V'_{3n}-\frac{\sin\lambda}{r_3}V_{3n}=0, \quad -\frac{n}{r_3}X_{3n}+\Theta'_{3n}-\frac{\sin\lambda}{r_3}\Theta_{3n}=0,\\
&-G^{*}U_{1n}+\left(\frac{r_1}{r_2}A_{55}^{(1)}-\frac{h_1}{2}G_c\right)X_{1n}+G^{*}U_{3n}+\left(\frac{r_3}{r_2}A_{55}^{(3)}-\frac{h_3}{2}G_c\right)X_{3n}+\left(\frac{r_1}{r_2}A_{55}^{(1)}+h_2G_c+\frac{r_3}{r_2}A_{55}^{(3)}\right)W'_{n}=0.
\end{aligned} \tag{B.3}
$$